TECHNICAL ARTICLE

On the Fidelity of the Scaling Laws for Melt Pool Depth Analysis During Laser Powder Bed Fusion

M. Naderi[1] · J. Weaver[2] · D. Deisenroth[2] · N. Iyyer[1] · R. McCauley[3]

Abstract

In additive manufacturing, the part quality is highly dependent on process parameters. The morphology of the melt pool (depth and width) is highly affected by process parameter selection. Available scaling laws more or less overestimate or underestimate melt pool dimensions with the similar order of magnitudes in the errors. Depending on melt pool mode, either conduction or keyhole, and moving from one material to another, scaling laws might not perform well. To further analyze the performance of the available scaling laws, in this work, melt pool depth obtained from experiments is tested against three well-known scaling laws. The fidelity and error associated with the scaling laws are analyzed and discussed. To improve the accuracy of the prediction, we revised three scaling laws and the results are discussed. While in some cases the scaling laws might have reasonable errors roughly lower than 50%, in other cases, errors are very high signifying missing physics from the predictions. The revised version of the scaling laws improves the fidelity of the predictions. The analysis shows a careful attention is required when using scaling laws to avoid high percentage of error.

Keywords Scaling law · Melt pool depth · Laser powder bed fusion · Additive manufacturing

Introduction

The quality of additively manufactured (AM) parts using laser powder bed fusion (LPBF) is highly dependent on process parameters such as laser power (P), scan speed (u), laser beam diameter ($D4\sigma$ with σ as variance of Gaussian intensity profile), hatch spacing, scan direction and powder layer thickness , and thermophysical properties. The best selections of these parameters, which often require intensive multiobjective optimization, dictate the fate of the AM part in terms of porosity level, residual stress, anisotropy, and mechanical properties. The morphology of the melt pool (depth and width) is consequently affected by these selections. Either computationally expensive micro/meso/macro-scale simulations or simple analytical approaches are usually used to replace expensive trial-and-error experimentation to develop AM process maps by relating process parameters to melt pool characteristics. Numerical modeling has been widely used for process parameter effects on melt pool morphology, albeit with heavy computational cost. Computational approaches might therefore be insufficient for fast optimization. To accelerate parameter selections and AM process mapping, analytical/semi-analytical approaches are highly desirable as alternatives for time-consuming experimental and computational work. Linear or volumetric energy density demonstrates the effect of various parameters (i.e., laser power, scan speed, hatch spacing, and layer thickness) on meltpool geometries and the part performance [1–5]. However, these approaches are not applicable for a broad range of LPBF parameters and may not correlate well from one material and machine to another [6]. Also, the effect of thermophysical properties and laser spot diameter are missing from these approaches [7]. Hence, scaling laws considering thermophysical properties and dimensional analysis have been emerged in the AM community. [8–13].

The research articles pertaining to process parameter selections and scaling melt pool geometry using analytical methods are abundant in the literature. These scaling laws articles aim to correlate the experimental measured

✉ M. Naderi
  mnaderi@tda-i.com

1 Technical Data Analysis, Inc. (TDA), 3190 Fairview Park Dr, Falls Church, VA 22042, USA

2 National Institute of Standards and Technology, Engineering Laboratory, Gaithersburg, MD, USA

3 US Naval Air Systems Command, Patuxent River, MD 20670, USA

quantities and explain the effects of varying process parameters on final part performance using dimensionless parameters and simple thermal models. Among them, for instance, Hann et al. [8] proposed a relationship between normalized melt pool depth and normalized enthalpy. While the former refers to the ratio of the melt pool depth to the laser spot diameter, the latter refers to the ratio of deposited energy to the enthalpy of melting. Two normalized numbers can describe the transition from conduction to keyhole mode. King et al. [9] showed that the plot of normalized melt pool depth versus normalized enthalpy collapses to a useful curve to identify the transition from conduction to keyhole mode. They observed that the transition from conduction to keyhole mode occurs around a normalized enthalpy ($\Delta H/h_s$) of 30 ± 4 for 316L stainless steel with powder layer thickness of 50 μm. Rubenchik et al. [11] applied the Eagar and Tsai [14] model to obtain the thermal distribution in a LPBF conduction mode and found a scaling law for melt pool depth, width, and length from simulations and experiments. Ye et al. [13] combined the work of King et al. [9] and Rubenchik et al. [11] and included a variable absorption coefficient from conduction to keyhole mode. They introduced a normalized thermal diffusion length similar to thermal diffusion depth of Rubenchik et al. [11] and proposed normalized depth as a function of normalized enthalpy and normalized thermal diffusion length. These dimensionless numbers can be derived from a dimensionless analysis using the Buckingham π theorem [15]. Using Buckingham π theorem, Fabbro [12] used an approach based on an energy balance equation and derived an analytical model that gives the evolution of the keyhole depth as a function of the operating parameters and the thermophysical properties. Groβmann et al. [16, 17] performed dimensional analysis for single and two melt track and estimated the melt pool width using a scaling law, which is valid for certain regions of process parameters. Later, Yang et al. [18] extended the model developed by Groβmann et al. [16] to consider laser beam size independency into the scaling law for melt pool width estimation. Weaver et al. [7] investigated the influence of the spot size effects on the melt pool morphology and the use of scaling laws to explain the influence on the melt pool depth for IN625. They compared melt pool depth estimated from three scaling laws developed by Rubenchik et al. [11], Ye et al. [13] and Fabbro [12]. They also noticed that melt pool depth from all three scaling laws is highly dependent on the absorption coefficient and predicted melt pool depth showed around 50% errors, with some cases around 100%. Gan et al. [19] scaled melt pool aspect ratio with a "keyhole number" as normalized enthalpy and investigated keyhole stability and porosity development. It should be noted that the depth from Gan et al. [19] is the vapor depression depth, which is not the same as the melt pool cross-sectional depth. Coen et al. [20] incorporated the analytical models of Rubenchik et al. [11] for conduction mode and Fabbro [12] for keyhole mode to predict melt pool width and depth for Ti64V, SS316L, and In718. Simonds et al. [21] performed tests on Ti64 and used direct real time measurements to quantify the relationship between melt pool geometry and energy absorption. Mukherjee et al. investigated the influences of process parameters and alloy properties (Ti64, SS316L, In718) on the structure and properties of AM parts using four dimensionless numbers [2]. Yang et al. derived an improved dimensionless scaling law to correlate the meltpool width with material and process parameters. They performed experimental measurements and finite element models to validate the derived law [18]. Using dimensionless analysis, Wang and Liu [22] proposed four key dimensionless numbers to characterize the thermodynamical behaviors during selective laser melting process. Hanemann et al. used normalized enthalpy to correlate meltpool width and depth with processing parameters considering the effect of scan direction and base plate location [10] during LPBF. Using Fabbro's model [12] and high-speed camera image, Goossens and Brecht Van extracted meltpool width from images and estimated meltpool depths for LPBF of SS316L by multiplying meltpool width with meltpool aspect ratio [23]. Liu et al. [24] used an analytical model to predict molten pool geometry by establishing a heat balance within the front part of the molten pool for Ti64V. Their analytical model was validated through experiments and numerical simulations. Rankouhi et al. [25] presented two dimensionless numbers correlating process parameters to the density considering the Buckingham π theorem and the implementation of a matrix transformation method. In a recent review paper, Agrawal et al. [26] reviewed existing analytical equations and models that provide an estimate of the melt pool geometries as a function of material properties.

The above review shows analytical-based scaling laws have been widely used in the literature, and predictions for a wide range of parameters, and the accuracy of reported melt pool dimensions available in the literature are unsatisfactory and inconsistent. In this paper, we aim to compare some of the available scaling laws based on the works of [8, 9], analyze the error associated with their predictions, and suggest a scaling law differentiating conduction and keyhole modes. We compare three methods including Rubenchik et al. [11], Fabbro [12], and Ye et al. [13] with a variety of data obtained from different sources available in the literature. We chose these three scaling laws because they are popular scaling laws that account for the laser beam size and thermophysical properties. We then slightly revise the available scaling law differentiating conduction and keyhole modes.

Background Overview

Scaling laws based on simple analytical approaches can be used to estimate melt pool dimensions. Among several scaling laws available in the literature for melt pool dimension estimation, we briefly describe the models proposed by Rubenchik et al. [11], Fabbro [12], and Ye et al. [13]. All three methods consider a dimensionless parameter called normalized enthalpy, $\Delta H/h_s$, which was initially defined by Hann et al. [8]. The normalized enthalpy is written as follows.

$$\frac{\Delta H}{h_s} = \frac{AP}{\rho C(T_m - T_0)\sqrt{\pi D u \sigma^3}} \tag{1}$$

where P is laser power, u is scan speed, ρ represents powder density, C is specific heat, T_m is powder melting temperature, T_0 stands for initial substrate temperature, D represents thermal diffusivity, σ is laser spot size, and A is material absorption coefficient. In the above equation, the enthalpy of melting is defined as $h_s = \rho C(T_m - T_0)$ [7]. In Eq. (1), thermal diffusivity is defined as $D = \kappa/(\rho C)$, where κ is thermal conductivity. In this work laser spot diameter and radius are 4σ and 2σ, respectively, with σ as the variance of Gaussian intensity profile. Also, the laser power profile is assumed having a Gaussian profile for all the data considered in this work.

Rubenchik et al. [11] Model

Following Hann et al. [8] and King et al. [9], Rubenchik et al. [11] applied the Eagar and Tsai [14] model to obtain the thermal distribution in a LPBF conduction mode as follows.

$$\rho C \frac{\partial T}{\partial x} + \nabla \cdot \kappa \nabla T = 0 \tag{2}$$

with the boundary condition of

$$\kappa \frac{\partial T}{\partial z} = AIf(x, y) \tag{3}$$

where T is temperature, $I = P/(\pi(2\sigma)^2)$ represents laser irradiance, and $f(x, y)$ is a two-dimensional Gaussian beam shape. Rubenchik et al. [11] defined a thermal diffusion length δ as

$$\delta = \sqrt{\frac{D \cdot \sqrt{2}\sigma}{u}} \tag{4}$$

They then demonstrated that the temperature distribution in a melt pool can be specified with two dimensionless parameters: B and p. Using regression analysis by fitting the melt pool depth, length, and width as a function of B and p, they proposed a universal polynomial function. Using the plot of melt pool depth normalized by thermal diffusion length, d/δ, versus normalized enthalpy, Rubenchik et al. [11] observed that test data for steel, Ti6Al4V, and IN625 collapsed on a linear curve with the slope of $\cong 0.25$. This empirical relationship can be expressed as:

$$\frac{d}{\delta} = 0.25\frac{\Delta H}{h_s} \tag{5}$$

It is noted that Rubenchik et al. [11] used $\sqrt{2}\sigma$ instead of 2σ throughout the derived equations. In Eq. (5), the constant, 0.25, is extracted from Fabbro's analysis of Rubenchik's data [12]. Fabbro [12] analyzed the normalized melt pool depth ($d/2\sigma$) versus normalized enthalpy ($\Delta H/h_s$). Using a linear fit equation of $Y = Y_0 + \alpha(X - X_0)$ with the assumptions of $X_0 \approx 25 - 30$, $Y_0 \approx 2$ for keyhole (KH) mode and $X_0 \approx 10$, $Y_0 \approx 0$ for conduction mode extracted from the original data of King et al. [9], he found the slope of $\alpha \approx 0.25$ for the linear fit.

Fabbro [12] Model

Fabbro [12] used energy conservation inside a cylindrical keyhole based on the laser welding literature and derived an analytical model describing the evolution of the keyhole depth as a function of the operating parameters and the thermophysical properties of the powder material. He showed that the solution of heat transfer analysis inside the keyhole configuration can be described by only three independent dimensionless parameters. According to Fabbro [12], there exists a linear relationship among three dimensionless parameters including $\Pi_1 = d/(4\sigma)$, $\Pi_2 = Pe$, and $\Pi_3 = AP/(4\sigma\kappa(T_v - T_0))$. The first parameter is depth to laser spot radius, the second one is Peclet number, and the third one is the ratio of two powers [12]. According to Buckingham Π theorem, we can relate three dimensionless parameters as [12]:

$$\Pi_1 = f(\Pi_2, \Pi_3) \tag{6}$$

Fabbro developed in the following equation to relate three dimensionless parameters:

$$\frac{d}{4\sigma} = \frac{AP}{4\sigma\kappa(T_v - T_0)(mPe + n)} \tag{7}$$

where T_v is boiling or evaporation temperature. Two empirical constants m and n are 2.4 and 3, respectively, for $2 \leq Pe \leq 10$. The above equations are derived based on the assumptions that the governed process is in keyhole mode where the recoil pressure generates a cylindrical void about the size of the laser beam diameter with the inner wall temperature as the boiling temperature. Similar to Weaver et al.

[7], high absorption coefficient of 0.8 is used in Fabbro's model, since this model is based on laser welding, which primarily works in keyhole mode. Equation (7) can be written as the following [12].

$$\frac{d}{4\sigma} = \frac{R_0}{1 + \frac{u}{V_0}} \tag{8}$$

with $R_0 = \frac{AP}{n(4\sigma)\kappa(T_v - T_0)}$ and $V_0 = 2\frac{n}{m}\frac{\kappa}{4\sigma\rho C}$;for usual LPBF parameters, one can show $u >> V_0$ and Eq. (8) can be written as:

$$\frac{d}{4\sigma} = \frac{R_0 V_0}{V} \tag{9}$$

Equation (9) can be converted to Rubenchik's dimensionless parameters of d/δ and $\Delta H/h_s$ as follows.

$$\frac{d}{\delta} = \frac{\pi^{1/2}}{2^{3/4}} \frac{1}{2Pe^{1/2}} \frac{T_m}{m(T_v - T_0)} \frac{\Delta H}{h_s} \tag{10}$$

Ye et al. [13] Model

The highlight of Ye et al. [13] work is to consider a non-constant absorption coefficient in the scaling law using an empirical fit to calorimetry-based laser energy absorption measurements for different laser parameters. The melt pool behavior strongly depends on the process parameters during LPBF. The combination of the process parameters can establish either conduction mode or keyhole mode [27]. Within a certain combination of process parameters, the melt pool heats up excessively, and vaporized materials impose recoil pressure on the molten pool and a keyhole (cavity) forms [9]. The keyhole caused by vaporization-induced recoil pressure increases the laser absorption process. Therefore, models considering non-constant absorption coefficient might reflect somehow the influence of the recoil pressure especially during the keyhole regime. Laser energy absorption increases with the transition from conduction mode to keyhole mode due to multiple reflections inside the cavity or keyhole [13, 28–30]. Ye et al. [13] proposed a normalized enthalpy, β, considering non-constant absorption, A_e, and normalized thermal diffusion length, L_{th}, after combining the work of King et al. [9] and Rubenchik et al. [11] as follows.

$$L_{th} = \frac{\delta}{2\sigma} = \frac{1}{\sqrt{Pe}} \tag{11}$$

$$\beta = \frac{A_e P}{\pi h_s \sqrt{Du(2\sigma)^3}} \tag{12}$$

where Pe is Peclet number ($Pe = u2\sigma/D$). Considering two above dimensionless parameters, Ye et al. [13] found the

existence of a linear relationship between the depth-to-spot radius ratio ($d/(2\sigma)$) and the normalized thermal diffusion length multiplied by normalized enthalpy through an empirical constant $K_0 = 0.6$.

$$\frac{d}{2\sigma} = K_0 \beta L_{th} \tag{13}$$

Note that the above equations proposed by Ye et al. can be derived from Buckingham Π theorem (Appendix A). The effective absorptivity, A_e in the above equation, can be expressed as follows [7].

$$A_e = \begin{cases} A_m & \frac{d}{2\sigma} \leqslant 1 \\ 0.7(1 - e^{-0.66\beta_{A_m} L_{th}}) & \frac{d}{2\sigma} > 1 \end{cases} \tag{14}$$

where A_m represents a constant absorption during conduction mode. The keyhole threshold in Eq. (14) is based on $d/(2\sigma)$ as defined by Weaver et al. [7]. Other equivalent thresholds can be used to differentiate conduction mode from keyhole mode. It is noted that the coefficient $K_0 = 0.6$ in Eq. (13) can be derived from Fabbro's equation (10). One can relate the normalized $\Delta H/h_s$ to normalized β through $\Delta H/h_s = \sqrt{\pi}2^{3/2}\beta$ and substitute into Eq. (9) to derive the following relationship among $d/2\sigma$ and β and L_{th}.

$$\frac{d}{2\sigma} = \pi \frac{T_m - T_0}{m(T_v - T_0)} \beta L_{th} = K_0^* \beta L_{th} \tag{15}$$

Note that the above equation is derived based on the definition of ΔH of Eq. (1) and assumes the laser spot diameter is equal to 4σ. Slightly different from Eq. (10), we considered the effect of initial substrate temperature (T_0) within h_m. If one uses roughly the average value of the melting and boiling temperature reported in Table 1, coefficient $K_0^* \approx 0.6$ which is compatible with K_0 of Eq. (13).

Materials and Experiment

In this work, two materials including IN625 and IN718 are used for LPBF testing and melt pool measurements. For nickel superalloy 625 (IN625), two different LPBF machines including an EOS M270 and a custom research platform named the additive manufacturing metrology testbed (AMMT) [7, 31] were used.[1] An EOS M270 machine was used to create tracks at four laser powers (122 W, 179 W, 150 W, and 195 W), four laser scan speeds (200 mm/s,

---

[1] Certain commercial equipment, instruments, or materials are identified in this paper in order to specify the experimental procedure adequately. Such identification is not intended to imply recommendation or endorsement by NIST, nor is it intended to imply that the materials or equipment identified are necessarily the best available for the purpose.
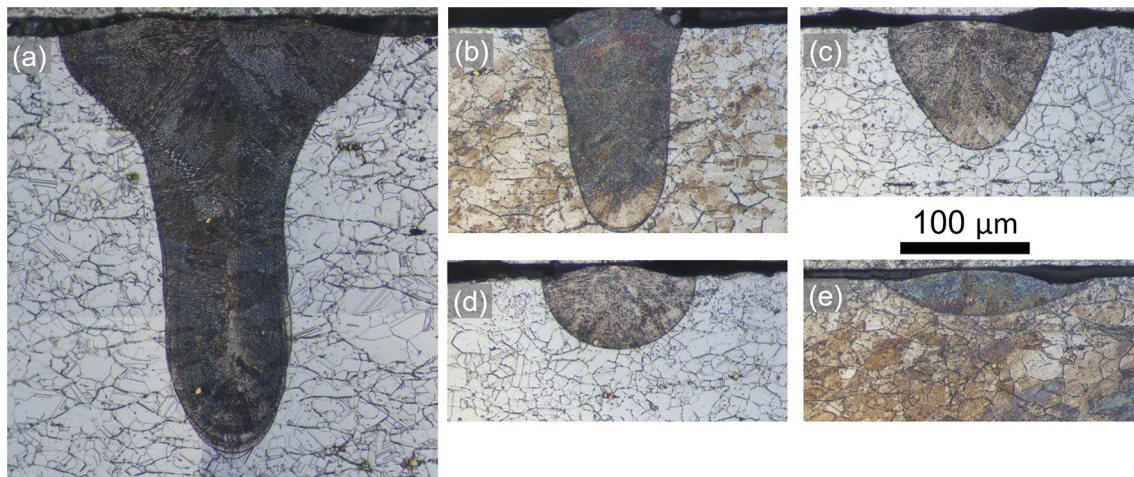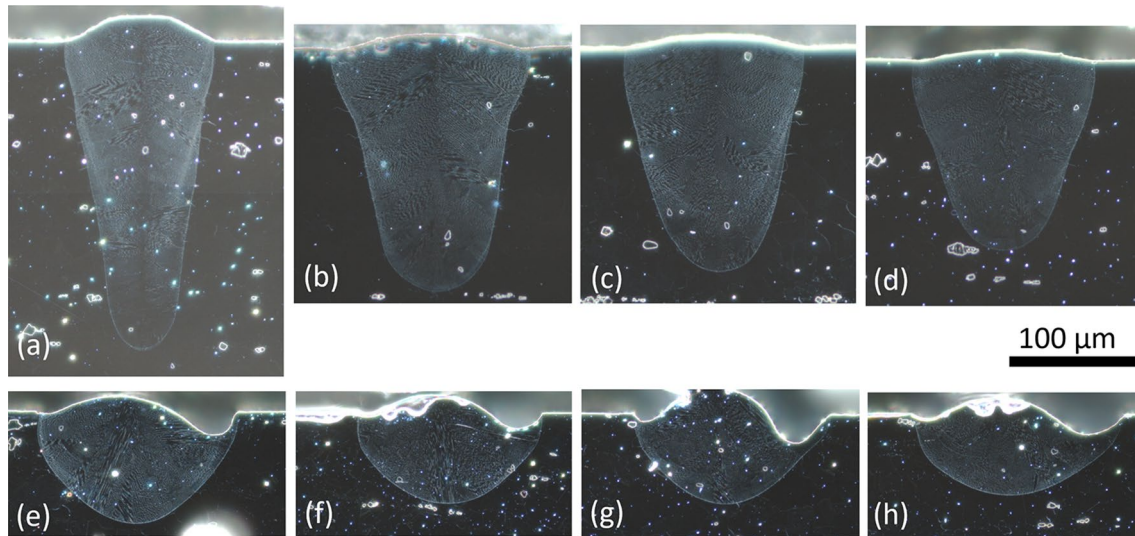
Fig. 1 Bright field optical micrographs of melt pool cross sections on IN625 ranging from deep keyholing to conduction mode. The laser power, speed, and Gaussian spot diameter are: **a** 195 W, 200 mm/s, 100 µm, **b** 195 W, 800 mm/s, 50 µm, **c** 195 W, 800 mm/s, 100 µm, **d** 195 W, 800 mm/s, 118 µm, **e** 195 W, 800 mm/s, 256 µm

400 mm/s, 800 mm/s, and 1200 mm/s), and spot diameters ranging from 80 µm to 322 µm. Not every combination was produced. The NIST (National Institute of Standards and Technology) AMMT was used to create tracks at 195 W, 800 mm/s, and spot diameters ranging from 50 µm to 256 µm. The laser spot diameter is the $D4\sigma$ diameter, which is approximately equivalent to the Gaussian diameter since the power distributions for both LPBF machines are nominally Gaussian. The laser spot diameter for the EOS machine was estimated based on machine specifications. The spot size was varied by using the machine's variable focus setting as well as by positioning the sample at different locations along the beam caustic. The AMMT laser spot size was measured by first attenuating the power by pulsing at 1/1000 duty cycle and placing neutral density filters in the collimated section of the optical path. The power distribution is then measured at the build plane by exposing the laser to a charge-coupled device (CCD) array. The measured power distribution was later verified using a commercial off-the-shelf laser beam sampler. Single tracks on IN625 substrates were produced and characterized with the same procedure described for IN718 substrates. More details are provided in the work of Weaver et al. [7]. Figure 1 shows several melt pool cross sections with different laser process parameters that range from deep keyholing to conduction mode.

For nickel superalloy 718 (IN718), an EOS M290 machine was used to create tracks at 285 W, 960 mm/s, and spot diameter of 80 µm. The AMMT of the NIST was used to create tracks at three laser powers (245 W, 285 W, and 325 W), three laser scan speeds (800 mm/s, 960 mm/s, and 1200 mm/s), and several spot diameters ranging from 48 µm to 131 µm. The laser spot diameter is the Gaussian diameter, which is approximately equivalent to the $D4\sigma$

since the power distributions for both LPBF machines are nominally Gaussian. The laser power of both machines was measured with calibrated thermal power meters with a standard measurement uncertainty (k = 2) of ±5%. The scan speed was measured via high-speed imaging of the melt pool and for both machines is estimated to have a standard measurement uncertainty of ±2.5%. The laser spot diameter for the EOS machine was estimated based on machine specifications. The laser spot diameter for the AMMT was measured with the laser operating at ≈ 100*W* at a low duty cycle (100 µs pulses at 5 Hz) and high attenuation (optical density of > 10). The laser was focused onto a windowless focal plane array positioned on the build plane. The laser spot diameter was changed by calibrating the default position of the inline dynamic focusing lens. The laser spot diameter standard measurement uncertainty is estimated to be ±8%. Single-track laser scans were made on IN718 substrates (25.4 mm×25.4 mm×3.175 mm). The surface was ground with 320 grit paper to create a uniform matte finish. Tracks were at least 10 mm in length and cross-sectioned perpendicular to the scan direction. Most tracks were cross-sectioned at the approximate center along the scan direction. Some tracks were cross-sectioned at multiple locations along the scan direction. No dependence on location for melt pool depth and width was observed in these cases. The variation in depth and width along the scan direction are estimated to be 5% and 2%, respectively (see Appendix B). Cross sections were metallographically prepared and etched with aqua regia (1 part nitric acid to 3 parts hydrochloric acid). The melt pool depth and width were measured using bright field or dark field optical microscopy. The depth is measured perpendicular to the top surface and defined as the greatest

Fig. 2 Dark field optical micrographs of melt pool cross sections on IN718 ranging from deep keyholing to conduction mode. The laser power, speed, and Gaussian spot diameter are: **a** 285 W, 960 mm/s, 49 μm, **b** 285 W, 800 mm/s, 67 μm, **c** 325 W, 960 mm/s, 67 μm, **d** 285 W, 960 mm/s, 67 μm, **e** 285 W, 960 mm/s, 110 μm, **f** 245 W, 960 mm/s, 110 μm, **g** 285 W, 1200 mm/s, 110 μm, **h** 285 W, 960 mm/s, 131 μm

distance from the top surface to the bottom of the melt pool. The width is measured parallel to the top surface and defined as the widest distance of the melt pool. Figure 2 shows several melt pool cross sections with different laser process parameters that range from deep keyholing to conduction mode. About 160 melt pool depth measurements are discussed in the next section.

Results and Discussion

In this section, we first analyze the melt pool depth and the associated errors estimated from three scaling laws for our experimental data of IN625 and IN718. We plan to compare estimated melt pool depth against test data using the previously explained three scaling laws. We will then discuss a revised version of the scaling laws to improve the fidelity of the predictions. After that, we apply the proposed revised version of the scaling laws for two other materials, namely Ti6Al4V and SS316, with the data obtained from Ye et al. [13]. The scaling laws are according to Rubenchik et al. [11], Ye. et al. [13], and Fabbro [12]. For convenience, we will simply name these scaling laws Rubenchik, Fabbro, and Ye model later in this paper. Material properties are summarized in Table 1. The range of laser parameters for different tests are presented in Table 2.

**Table 1** Bulk material properties [7, 13, 20]

	IN718	IN625	Ti6Al4V	SS316L
$\rho(\text{kgm}^{-3})$	7727	8440	3920	8000
$C(\text{JKg}^{-1}\text{K}^{-1})$	650	720	830	830
$\kappa(\text{Wm}^{-1}\text{K}^{-1})$	29	28	33	31
$T_m(\text{K})$	1526	1563–1623	1877–1923	1633–1683
$T_v(\text{K})$	3070	3500	3573	3090
A_m	0.28	0.28	0.26	0.28

Table 2 Range of laser parameters [7, 13]

	IN718	IN625	Ti6Al4V	SS316L
$P(\text{W})$	245–324	30–300	30–550	30–520
$u(\text{mms}^{-1})$	800–1200	200–1200	400–1500	100–1500
4σ (μm)	48–131	50–322	60–100	15–300

Results of IN625

Melt pool depths and percent difference (or error) are estimated using previously mentioned scaling laws as presented in Fig. 3a, b, respectively. The solid line on Fig. 3a is the linear fit line. The percent difference or error is the absolute difference between calculated and measured depth divided by the measured depth, $|(d_{test} - d_{sim})/d_{test}|$. Absorption coefficient of 0.4 is used in the Rubenchik model. A high absorption coefficient of 0.8 is used in the Fabbro's model, since this model is based on laser welding, which primarily works in keyhole mode. For the Ye model, absorption

(a)

(b)
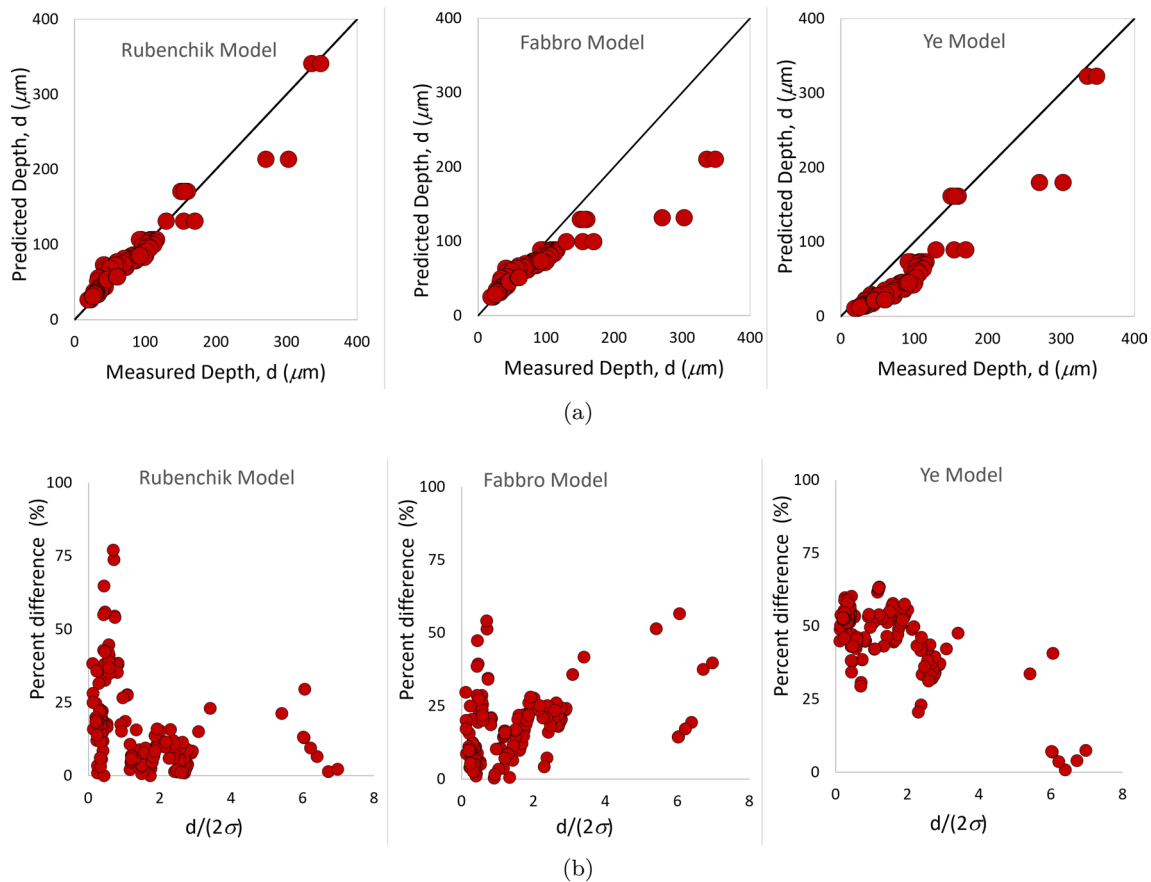
Fig. 3 **a** Estimated versus measured melt pool depth, **b** Percent difference between the predicted and measured melt pool depth versus the depth-to-spot radius ratio obtained from Weaver et al. [7] for IN625 using scaling laws of Rubenchik et al. [11], Fabbro [12], and Ye. et al. [13]. Percent difference for $d/2\sigma \lesssim 1$ represents conduction mode, while percent difference for $d/2\sigma \gtrsim 1$ represents keyhole mode

coefficient function of Eq. (14) with minimum absorption of $A_m = 0.28$ is used. As seen in Fig. 3a, calculated depth based on Rubenchik is qualitatively more compact than calculated depth based on Fabbro and Ye model. For calculated data based on the Fabbro model, the reason can be attributed to the range of applicability for Peclet number, which is from 2 to 10. The range of Peclet number for measured data points is 2.1 to 27.2. Deviation from test data is even worse for calculations based on the Ye model compared to the Fabbro model with a shift in the curve at the keyhole transition. Analyzed errors presented in Fig. 3b provide information regarding the accuracy of the scaling laws. The Rubenchik model provides better accuracy than other scaling laws. In the Rubenchik model, the majority of the errors are less than 20%, while in the Fabbro model, the majority of errors are less than 30%. Errors based on the Ye model is roughly around 50% and much higher than the two other models. The reason might be related to absorption coefficient asymptotic exponential fitting extracted from different data points of three different materials reported by Ye et al. [13]. Weaver

et al. showed that modifying the absorption function coefficients within reason improved the model predictions [7].

Discussion on Rubenchik and Fabbro Model

Several notes can be observed from error analysis presented in Fig. 3. (1) All three models have poor predictions, with high percentage of error for conduction regime when compared to the keyhole regime. Here $d/2\sigma \lesssim 1$ refers to conduction mode, while $d/2\sigma \gtrsim 1$ represents keyhole mode. It is assumed that the threshold between conduction and keyhole occurs at the aspect ratio $d/2\sigma \approx 1$. (2) Roughly around the border between conduction and keyhole regime, Rubenchik and Fabbro model seem to work better and for most cases produce errors below 50%. For high aspect ratios, the error even gets smaller particularly for Rubenchik models. (3) There is a knee-type trend in errors associated with Fabbro's model. Moving away from the border between conduction and keyhole regime and for high aspect ratios ($d/2\sigma \gtrsim 4$), the errors associated
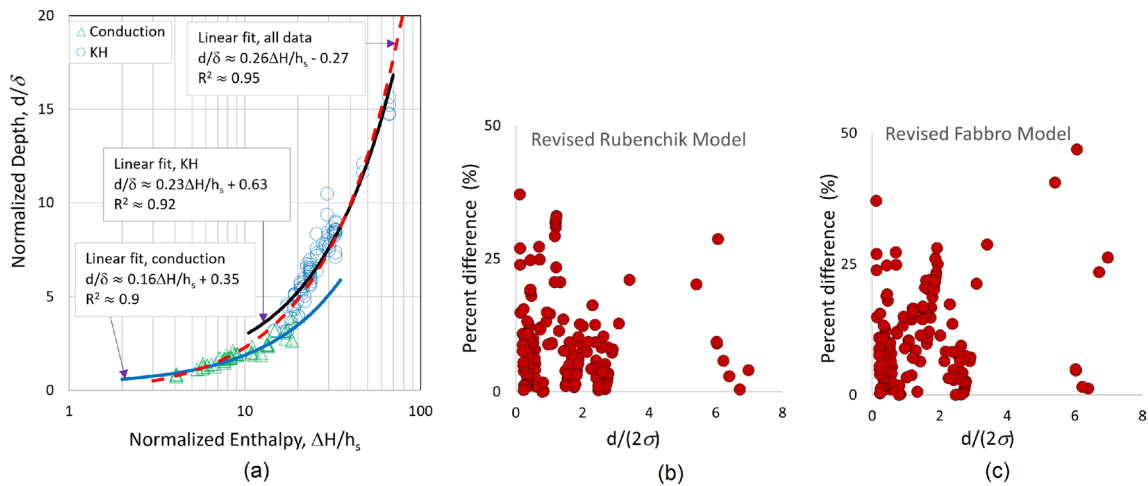
Fig. 4 **a** Semilog plot of normalized melt pool depth as a function of normalized enthalpy for IN625, and revised version of percent difference between the predicted and measured melt pool depth versus the depth-to-spot radius ratio for based on **b** revised Rubenchik model, **c** revised Fabbro model. Note that the linear fit appears curved in the semilog scale

with this model increase toward a steady level of the error. The reason could be related to the recoil pressure imposed on the keyhole (cavity) which pushes away molten metal from the keyhole and increases the laser absorption. To improve the predictions, we first discuss the threshold between conduction and keyhole mode in a normalized enthalpy type graph following the work of King et al. [9] and Fabbro [12]. We then revise the predictions using newly established relationships.

The semilog plot of normalized melt pool depth (d/δ) versus normalized enthalpy ($\Delta H/h_s$) is presented in Fig. 4a for IN625. The semilog plot is provided for better visualization of the conduction and keyhole region. While fitting a line for each mode, we extended the threshold roughly from $\pm 10 - 20\%$ where $'+'$ is for conduction mode and $'-'$ is for keyhole mode to assure the transition from conduction to keyhole is fairly captured. Green triangles are representative of conduction mode, while blue circles are representative of keyhole mode. The dashed red line is the linear fit on all the data points regardless of conduction and keyhole mode. Black and blue solid lines are the linear fit on keyhole mode data points and conduction mode data points, respectively. Fabbro [12] showed that with $m \approx 2.5$, $T_v \approx 3100$, $T_m \approx 1800$, and $T_0 \approx 300$, the slope of ≈ 0.27 can be derived, which is close to the value of 0.25 as the slope of linear fit. The slope of the linear fit of all data points is ≈ 0.26, which is close to Fabbro's finding. The graph of linear fit on all data points cannot fit well the data conduction regime data points. That is why predictions based on a single linear fit with the slope of 0.25 result in high percentage of error. Hence, to lower the level of the errors especially in the conduction regime, we revise Rubenchik model with two linear fits, one for conduction mode and one for keyhole, as follows.

$$\frac{d}{\delta} = a_0 \frac{\Delta H}{h_s} + b_0 \tag{16}$$

where a_0 is the slope of linear fit and b_0 is y-intercept of the linear fit. Depending on the condition of $\frac{d}{2\sigma}$ either $\lesssim 1$ or $\gtrsim 1$, the slope a_0 and y-intercept b_0 of linear fit are adjusted. From Fig. 4, one can observe that most of the errors are related to the conduction region where the deviation of the linear fit to all data and to conduction region data is considerable. The slope of linear fit to all data points and to keyhole regime is close the slope of 0.25 of Eq. (5). Hence, the percent of error for keyhole mode remains less affected. Decomposing the linear fit of all data point into conduction and keyhole linear fit improves the accuracy of the predictions and errors roughly fall below 30% for conduction mode as seen in Fig. 4b. The higher value of the slope slightly improve the fidelity of the predictions for higher aspect ratios in the keyhole regime. In contrast, the linear fit slope lower than 0.25 of Eq. (5) enhances the predictions. Table 3 summarizes the coefficients of linear fits of Eq. (16) along with their R^2.

Since the Fabbro model is mostly developed for the keyhole regime, we expect to observe more errors for the conduction mode. To improve the predictions and reduce the error in Fabbro's method for conduction regime, we employ the revised Rubenchik model of Eq. (16). For high aspect ratios, Fabbro-based predictions can be improved by increasing the absorptivity coefficient from 0.8 to 1. This can be explained by the knee type trend in the error which is discussed later. Recoil pressure at high aspect ratios where deep keyhole occurs helps to push molten materials on the side of the cavity and maximize the absorptivity at the bottom of the keyhole. We therefore

Table 3 Coefficients of the linear fits for revised Rubenchik model

	Linear fit on conduction region			Linear fit on keyhole region			Linear fit on all data		
	a_0 (variation range)	b_0 (variation range)	R^2	a_0 (variation range)	b_0 (variation range)	R^2	a_0 (variation range)	b_0 (variation range)	R^2
IN625	0.16 (0.148, 0.173)	0.35 (0.21, 0.49)	0.9	0.26 (0.24, 0.29)	−0.27 (−0.8, 0.26)	0.92	0.25 (0.24, 0.26)	−0.27 (−0.49, −0.045)	0.95
IN718	0.235 (0.22, 0.24)	−2.37 (−2.7, −1.97)	0.97	0.26 (0.24, 0.29)	−2.37 (−2.7, −1.97)	0.97	0.25 (0.24, 0.26)	−2.37 (−2.7, −1.97)	0.97
Ti64	0.12 (0.095, 0.13)	0.012 (−0.22, 0.26)	0.9	0.3 (0.29, 0.31)	−1.6 (−2.1, −1.2)	0.97	0.3 (0.29, 0.31)	−1.8 (−2.2, −1.5)	0.97
SS316L	0.12 (0.072, 0.18)	0.06 (−0.75, 0.87)	0.64	0.32 (0.29, 0.34)	−2.2 (−3.2, −1.2)	0.95	0.33 (0.31, 0.35)	−2.6 (−3.3, −1.8)	0.95

The range of variation has a confidence level associated with coefficient of determination (R^2)

Fig. 5 **a** Semilog plot of normalized melt pool depth ($d/2\sigma$) as a function of βL_{th}, **b** Revised percent difference between the predicted and measured melt pool depth versus the depth-to-spot radius ratio using revised Ye model for IN625
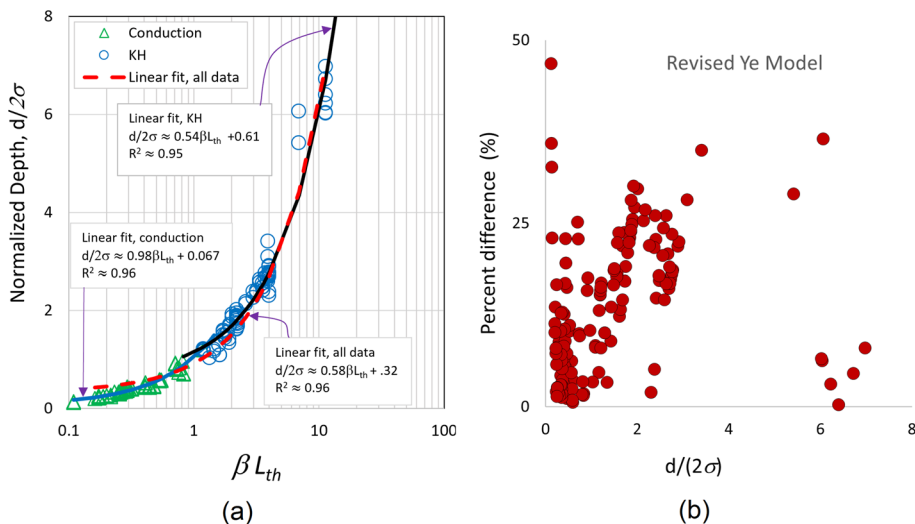
revise Fabbro's model to calculate the melt pool depth as follows:

$$d = \begin{cases} (a_0 \frac{\Delta H}{h_s} + b_0)\delta & \frac{d}{2\sigma} \lesssim 1 \\ \frac{AP}{\kappa(T_v - T_0)(mPe + n)} & \frac{d}{2\sigma} \gtrsim 1 \end{cases} \tag{17}$$

For $\frac{d}{2\sigma} \lesssim 1$, the absorption coefficient A takes the same value of 0.4 used in Rubenchik model. While, for $\frac{d}{2\sigma} \gtrsim 1$, the value of 0.8 of Fabbro model is used for the absorption coefficient before any steady state region. The threshold for the steady state region within the keyhole regime roughly takes place for aspect ratios $\gtrsim 5$ observed in the knee type trend of percent difference figures. Figure 4c shows the revised version of errors based on the above equation. It is seen that the percent difference graph and the level of the errors are improved especially for conduction and slightly for high aspect ratios. The level of the errors is decreased below 50%.

Discussion on Ye Model

Extending the above discussion to the Ye model, one can plot the normalized depth ($d/2\sigma$) versus the normalized thermal diffusion length (L_{th}) and normalized enthalpy (β) as seen in Fig. 5a. We plot the data on the semilog scale to have better visualization of conduction and keyhole mode. Similar to Fig. 4, we separated the data points for the conduction and keyhole regime based on the aspect ratio $d/2\sigma \approx 1$. Green triangles are representative of conduction mode, while blue circles are representative of keyhole mode. The dashed red line is the linear fit on all the data points regardless of conduction and keyhole mode. Black and blue solid lines are the linear fit on keyhole mode data points and conduction mode data points, respectively. The slope of linear fit on all data points and keyhole regime data points is 0.67 and 0.66 which are fairly close to value 0.6 seen as K_0 and K_0^* in Equations 13 and 15. In contrast, the slope of the conduction mode is 0.48, which is further from the value of 0.6.

Table 4 Coefficients of the linear fits for revised Ye model

	Linear fit on conduction region			Linear fit on keyhole region			Linear fit on all data		
	a_0 (variation range)	b_0 (variation range)	R^2	a_0 (variation range)	b_0 (variation range)	R^2	a_0 (variation range)	b_0 (variation range)	R^2
IN625	0.98 (0.93, 1.02)	0.067 (0.047, 0.086)	0.96	0.54 (0.51, 0.56)	0.61 (0.5, 0.72)	0.95	0.58 (0.57, 0.6)	0.32 (0.27, 0.38)	0.96
IN718	0.5 (0.49, 0.52)	0.19 (0.084, 0.29)	0.98	0.5 (0.49, 0.52)	0.19 (0.084, 0.29)	0.98	0.5 (0.49, 0.52)	0.19 (0.084, 0.29)	0.98
Ti64	0.55 (0.35, 0.74)	0.16 (−0.02, 0.34)	0.8	0.65 (0.63, 0.67)	0.4 (0.2, 0.6)	0.98	0.66 (0.65, 0.68)	0.27 (0.12, 0.42)	0.98
SS316L	0.56 (0.4, 0.72)	0.17 (0.005, 0.34)	0.8	0.69 (0.65, 0.74)	0.3 (−0.065, 0.64)	0.96	0.73 (0.69, 0.77)	0.1 (−0.16, 0.38)	0.96

The range of variation has a confidence level associated with coefficient of determination (R^2)
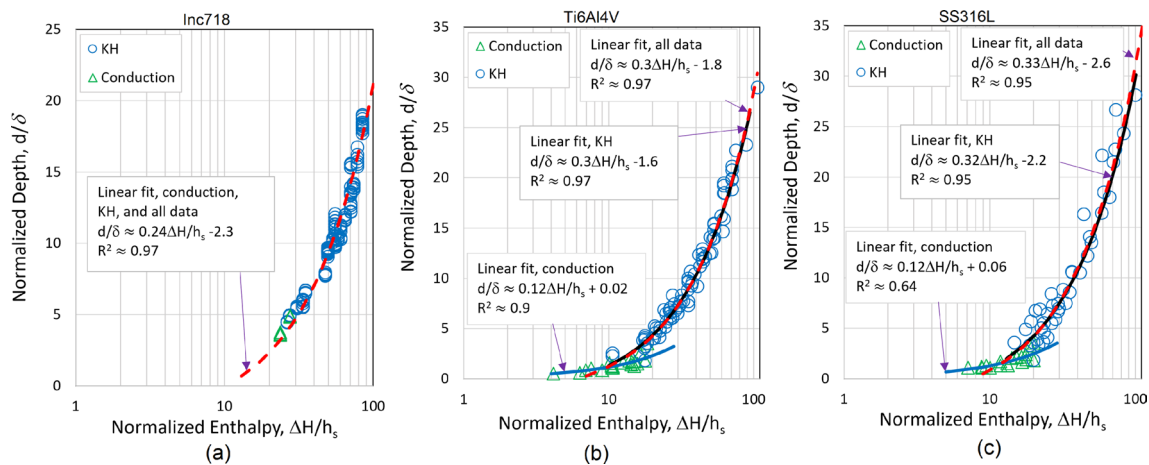
Fig. 6 Semilog plot of normalized melt pool depth as a function of normalized enthalpy for **a** IN718 of current work data, **b** Ti6Al4V of Ye et al. [13] data, **c** SS316L of Ye et al. [13] data

$$\frac{d}{2\sigma} = a_0 \beta L_{th} + b_0 \qquad (18)$$

where a_0 is the slope of linear fit and b_0 is y-intercept of the linear fit. Depending on the condition of $\frac{d}{2\sigma}$ either $\lesssim 1$ or $\gtrsim 1$, the slope a_0 and y-intercept b_0 of linear fit are adjusted.

As seen from Fig. 5b, the magnitude of the errors on the revised percent difference (error) are below 50% with a majority approximately lower than 30%. There are still a couple of data points with nearly 50% error. It is also seen that prediction improvements are not significant for high aspect ratio, since the slope of keyhole regime linear fits is close to slope of 0.6 in Ye et al. [13] model. Table 4 summarizes the coefficients of linear fits of Eq. (18) along with their R^2.

Results of IN718, Ti6Al4V, SS316L

Following the above discussion, in what follows we perform error analysis on the melt pool depth predictions utilizing both original and revised three scaling laws. The data of Ti6Al4V and SS316L are obtained from the work of Ye et al. [13] who carried out in situ optical absorptivity measurements in Ti6Al4V and stainless steel 316L as a function of incident laser power, scan velocity, and laser beam diameter. Laser power ranges from 30 W to 300 W, scan speeds are 500 mm/s, 1000 mm/s, and 1500 mm/s with laser beam radius in the range of 29–54 μm. Figure 6a–c presents semilog plot of normalized melt pool depth as a function of normalized enthalpy. Semilog plot of normalized melt pool depth ($d/2\sigma$) as a function of βL_{th} is plotted in Fig. 7a–c. Note that for IN718, the data corresponding to conduction region were about 10 out of 155 data point. Hence, due to the lack of data points for the conduction region, for this material, we consider only the linear fit on all data for error analysis rather than individual linear fits for conduction and keyhole. All the linear fits are based on Eqs. (16), (18), and (17). Tables 3 and 4 summarize the coefficients of linear fits along with their R^2. It is seen
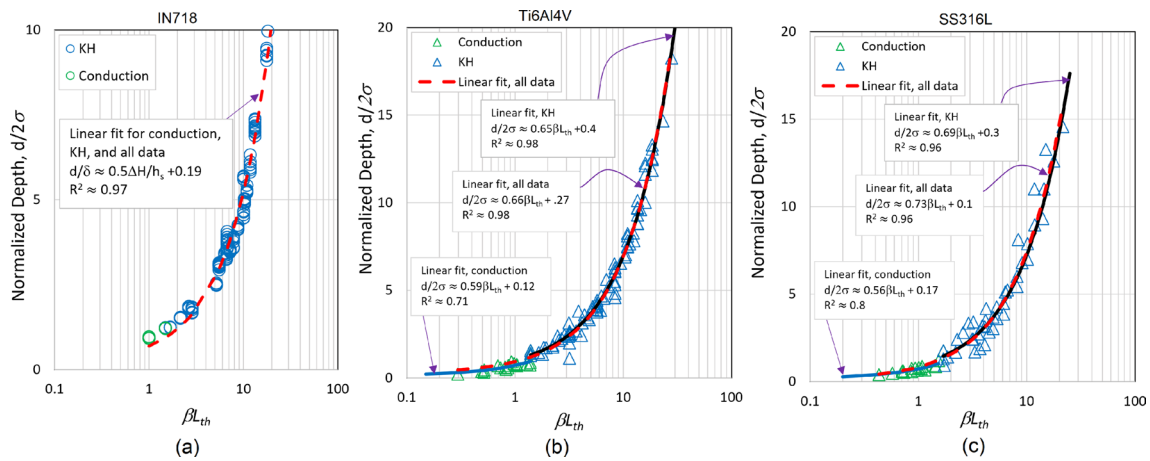
Fig. 7 Semilog plot of normalized melt pool depth ($d/2\sigma$) as a function of βL_{th} for **a** IN718 of current work data, **b** Ti6Al4V of Ye et al. [13] data, **c** SS316L of Ye et al. [13] data
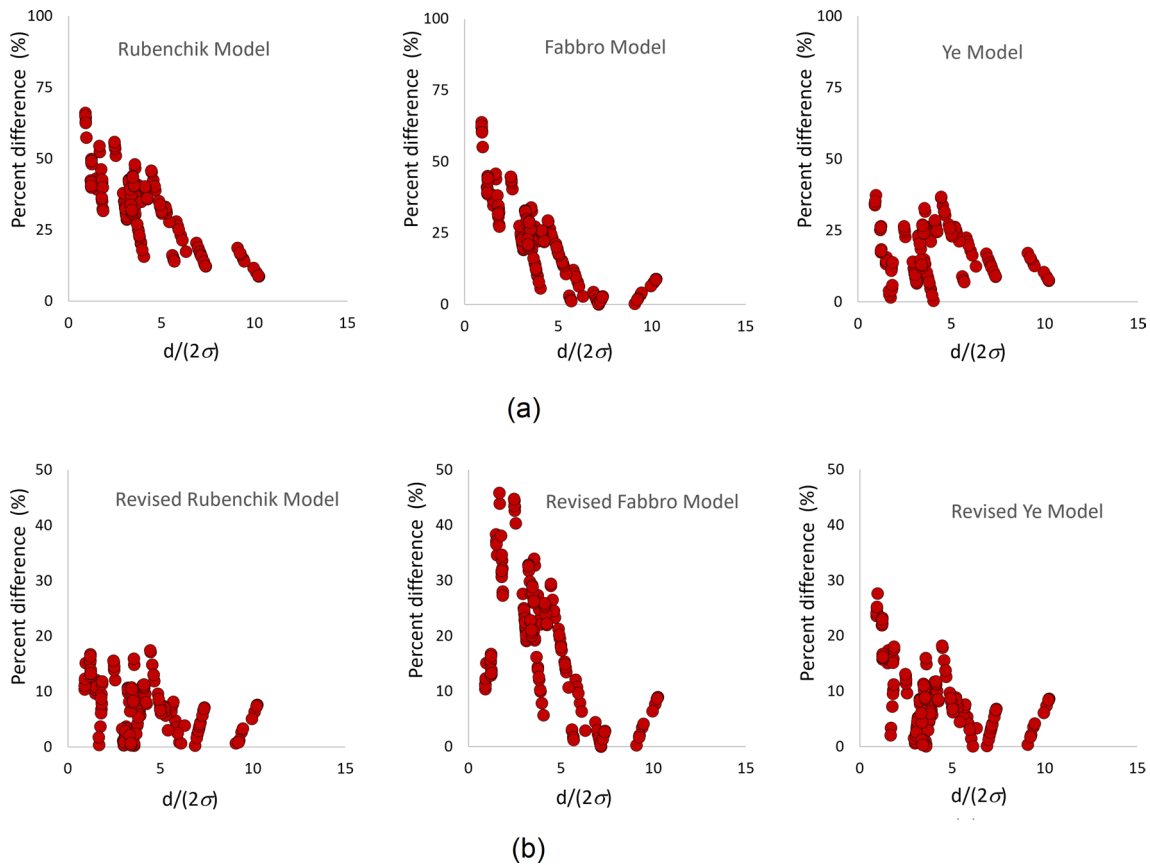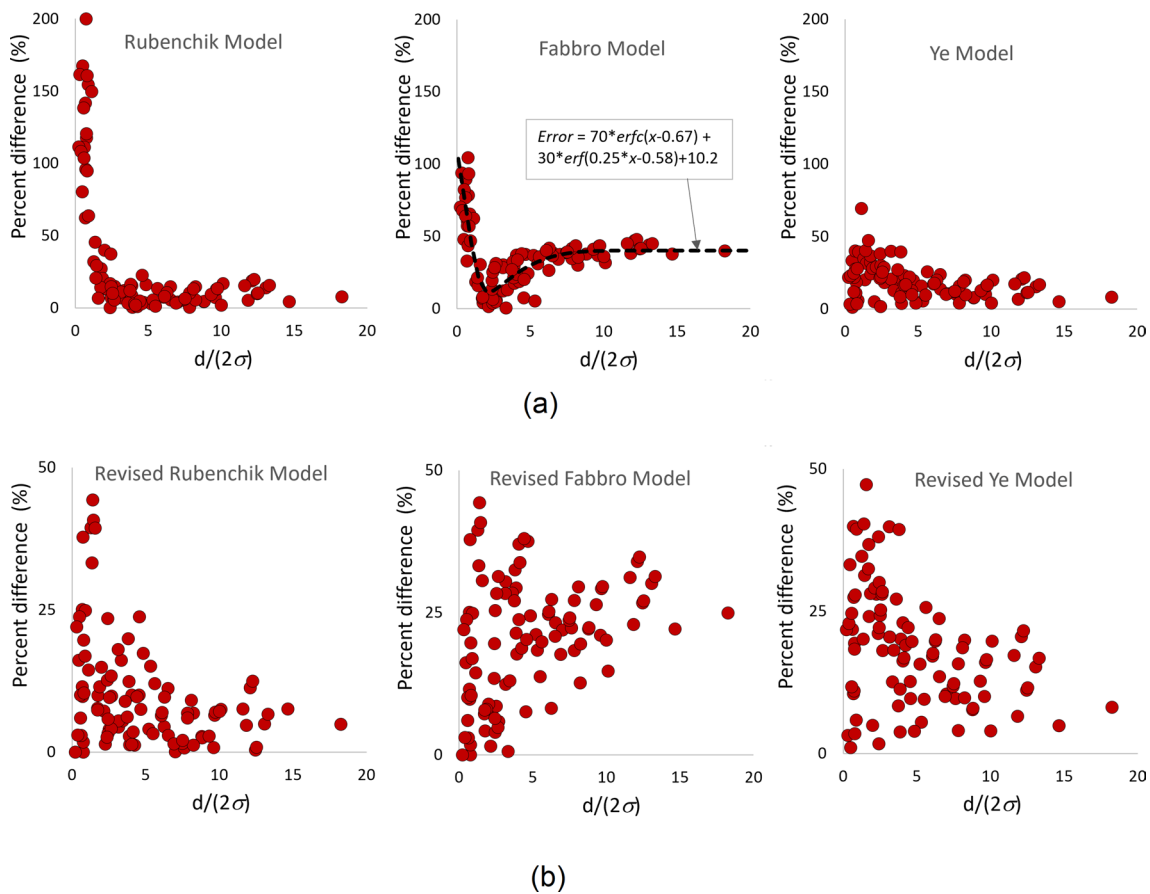

Fig. 8 Percent difference between the predicted and measured melt pool depth versus the depth-to-spot radius ratio for IN718 **a** using original Rubenchik, Fabbro, and Ye models, **b** using revised Ruben-chik, Fabbro, and Ye models. The percent difference is the absolute difference between the estimated and measured depth divided by the measured depth

that the slope of conduction and keyhole regime linear fits are very much different. Keyhole mode slopes have closer tendency toward the slopes of linear fits on all data compared to the conduction mode slopes.

Fig. 9 Percent difference between the predicted and measured melt pool depth versus the depth-to-spot radius ratio for Ti6Al4V data obtained from Ye et al. [13] **a** using original Rubenchik, Fabbro, and Ye models, **b** using revised Rubenchik, Fabbro, and Ye models. The percent difference is the absolute difference between the estimated and measured depth divided by the measured depth

IN718

The percent difference between original and revised three scaling laws is compared in Fig. 8 for IN718. Except the Ye model which produces errors lower than 50%, the two other models show a similar trend as observed in IN625. Using the revised version of the scaling law with two separate linear fits for each mode, the errors in the conduction regime are lowered below 30% for all models. For the Fabbro model, slight improvements are seen in the data of conduction mode while the rest of the data point are unaffected. The coefficients of linear fits for IN718 are summarized in Tables 3 and 4
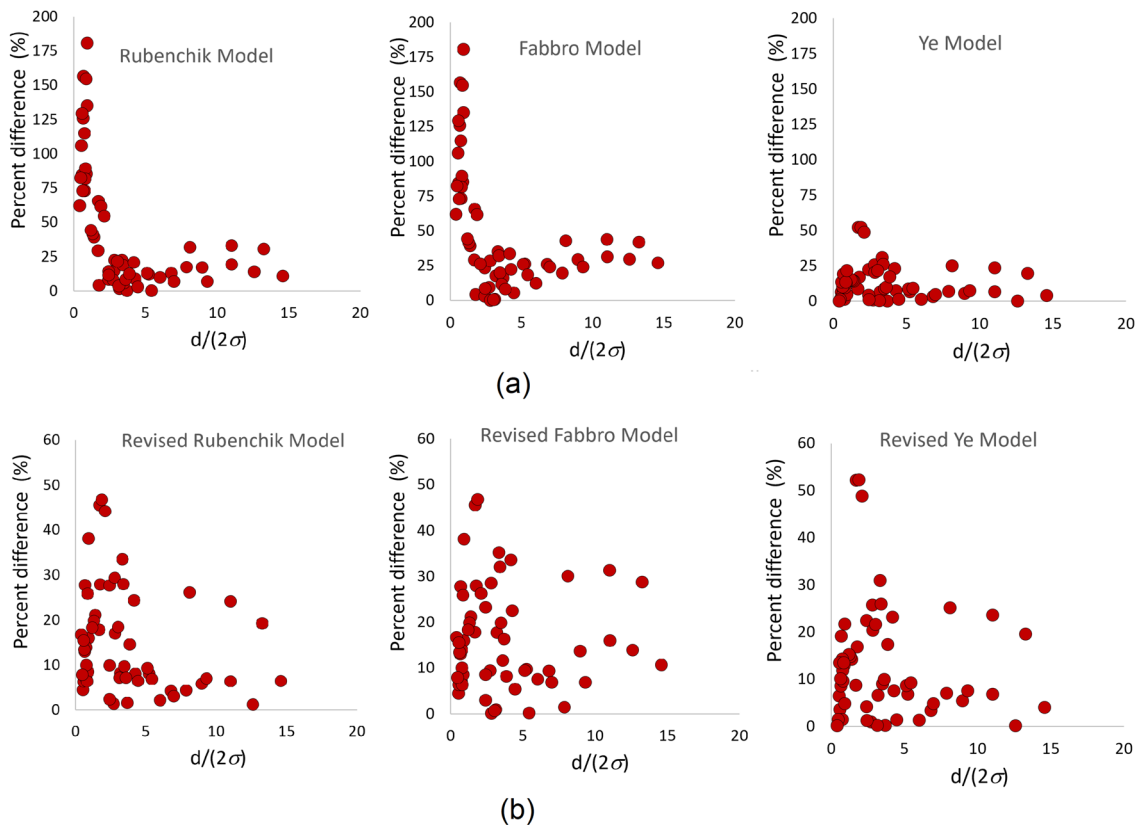
Ti6Al4V

Figure 9 compares the fidelity of original and revised version of three scaling laws for Ti6Al4v data points obtained from [13]. The percent difference of the Ye model is lower than Rubenchik and Fabbro models especially for conduction mode. Separating linear fits lowers the conduction regime

errors below 50% especially for Rubenchik and Fabbro models. Also, there is a clear knee-type trend in errors associated with the Fabbro model. The knee-type trend shows that error decreases around the border between the conduction and keyhole regimes. Moving toward keyhole regime and at high aspect ratios, the error reaches to a steady state stage, which might suggest the recoil pressure reaches a saturation level. This behavior can explain the maximum absorptivity coefficient of one considered for the steady state regime of the Fabbro model. These graphs, if represented by error functions, can signify the steady state region within the keyhole regime. By analyzing the knee type trend, one can express the knee type trend using an error function as follows:

$$Error \approx a_1 * erfc(x + a_2) + a_3 * erf(a_4 * x + a_5) + a_6$$

(19)

where *erf* and *erfc* are a Gaussian error function and its complementary function, defined as $erfc(x) = 1 - erf(x)$. The first term on the right hand side describes the descending part of the knee trend and the second term expresses the acceding part. Coefficients $a_1 - a6$ are correspondingly

Fig. 10 Percent difference between the predicted and measured melt pool depth versus the depth-to-spot radius ratio for SS316L data obtained from Ye et al. [13] **a** using original Rubenchik, Fabbro, and Ye models, **b** using revised Rubenchik, Fabbro, and Ye models. The percent difference is the absolute difference between the estimated and measured depth divided by the measured depth

70, $-0.67, 30, 0.25, -0.58$, and 10.2. The R-squared corresponding to this error function is about 0.7.

SS316L

Figure 10 compares the fidelity of original and revised version of three scaling laws for SS316L datapoints obtained from [13]. Similarly, the revised scaling laws improves the fidelity of the predictions by lowering the level of the errors. Note that the predictions from all three revised scaling laws discussed above are comparable, and any of them could be used from conduction to keyholing for meltpool depth analysis.

Conclusions

In this work, the fidelity of some available scaling laws including Rubenchik et al. [11], Fabbro [12], and Ye et al. [13] are evaluated. Melt pool depths are estimated and the percent differences or errors are assessed for three different materials including IN625, Ti64, and SS316L taken from

the literature and current experimental tests on IN718. The analysis showed that while the majority of the errors are below 50% for the keyhole regime, the errors associated with the conduction regime are roughly very high, particularly for Rubenchik and Fabbro models. It was seen that the Ye model produces errors qualitatively below 50%, except for some data points in conduction mode obtained from Weaver et al. [7] with above 50%. In an attempt to reduce the fidelity of the predictions and reduce the percentage of the errors, we carefully looked at the normalized melt pool depth (d/δ) versus normalized enthalpy ($\Delta H/h_s$) for Rubenchik and Fabbro models and the normalized melt pool depth ($d/2\sigma$) versus normalized enthalpy (β) times normalized thermal diffusion length (L_{th}). In a semilog plot, we defined two distinct linear fits for each conduction and keyhole regime. The revised version of the scaling law showed that the linear fits have lower slope in conduction mode than in keyhole mode. If combined with the Rubenchik model, the Fabbro model results in reasonable fidelity. While the revised Ye model improves the accuracy, the original Ye model should produce errors lower than 50%. Machine learning (ML) can be an alternative approach for the analysis of process

Table 5 Dimensional analysis table of parameters

	d	P	u	κ	ρC_p	ΔT	a
L	1	2	1	1	-1	0	1
M	0	1	0	1	1	0	0
T	0	-3	-1	-3	-2	0	0
Θ	0	0	0	-1	-1	1	0

parameters effects on the meltpool morphology. Comparison between scaling laws and ML remains a topic for our future work. The following conclusions are made.

1. Errors are inherent within the available scaling laws due to simplicity, lack of physics, or experimental errors propagating through the scaling laws. However, the magnitude of the errors could be reduced. Collapsing all the data of different material types weakens the fidelity of the predictions and might result in high error while generalized as a universal curve. Each material should be treated separately if high fidelity is desirable.
2. For the Rubenchik model, a separate linear fit for conduction and keyhole regimes lowers the errors and improves the accuracy. While using one linear fit for both conduction and keyhole regimes could fairly capture meltpool depth for high aspect ratios, it might worsen the predictions for the conduction regime.
3. The Fabbro model worked better if combined with the Rubenchik model. That is, for the conduction regime the Rubenchik model can be used. Also, a high absorption coefficient close to one can improve the accuracy of the predictions for high aspect ratios.
4. Similar to the Rubenchik model, separate linear fits based on the Ye model for conduction and keyhole regimes could result in better accuracy. Note that the Ye model usually produces errors lower than 50%. The revised version of the Ye model can be used if better accuracy is desirable.

Appendix A: Dimensional Analysis, Buckingham Π Theorem

Dimensional analysis as a powerful tool can identify the governing quantities of a system and allow for deriving simple connections among physical parameters. It is noted that a sufficient number of parameters should be considered for efficient analysis. The more the parameters, the less efficient is the dimensional analysis. Hence, for a LPBF process, only practical and important parameters need to be considered.

Suppose we plan to relate melt pool depth to laser power P, scan speed u, laser spot radius a, temperature difference $\Delta T = T_m - T_0$, thermal conductivity κ, and specific heat capacity ρC_p using the following function 20 representing the well-known Buckingham Π theorem.

$$d = f(P, u, \kappa, \rho C_p, \Delta T, a) \tag{20}$$

According to the above equation, the fundamental system of dimensions summarized in Table 5 is $[LMT\Theta]$ where L represents length, M is mass, T represents time, and Θ is temperature.

Equation (20) states that melt pool depth can be related to other parameters through dimensionless parameters Π_1, Π_2, and Π_3. Therefore, dimensional analysis can reduce the number of involved quantities from seven to three dimensionless parameters. Additional parameters such as hatch distance, recoil-pressure, surface tension, and layer thickness can be considered albeit with more complexity involved in the analysis. The relationship among the parameters can be described by solving the following equation and finding the null space of matrix $\mathbf{A}$ with:

$$\mathbf{A}\mathbf{x} = 0 \tag{21}$$

with

$$\mathbf{A} = \begin{bmatrix} 1 & 2 & 1 & 1 & -1 & 0 & 1 \\ 0 & 1 & 0 & 1 & 1 & 0 & 0 \\ 0 & -3 & -1 & -3 & -2 & 0 & 0 \\ 0 & 0 & 0 & -1 & -1 & 1 & 0 \end{bmatrix} \tag{22}$$

$$\mathbf{A}\mathbf{X} = \begin{bmatrix} 1 & 2 & 1 & 1 & -1 & 0 & 1 \\ 0 & 1 & 0 & 1 & 1 & 0 & 0 \\ 0 & -3 & -1 & -3 & -2 & 0 & 0 \\ 0 & 0 & 0 & -1 & -1 & 1 & 0 \end{bmatrix} \begin{bmatrix} d \\ P \\ u \\ \kappa \\ \rho C_p \\ \Delta T \\ a \end{bmatrix} \tag{23}$$

Equation (21) has infinite solution (X_n) in the null space as a linear combination of the solutions. Depending on the quantities of interest, three dimensionless parameters can be constructed through linear combination of the following vectors.

$$X_n = c_1 \begin{bmatrix} 1 \\ 0 \\ 1 \\ -1 \\ 1 \\ 0 \\ 0 \end{bmatrix} + c_2 \begin{bmatrix} 1 \\ -1 \\ 0 \\ 1 \\ 0 \\ 1 \\ 0 \end{bmatrix} + c_3 \begin{bmatrix} -1 \\ 0 \\ 0 \\ 0 \\ 0 \\ 0 \\ 1 \end{bmatrix} = c_1 x_1 + c_2 x_2 + c_3 x_3$$

(24)

To be consistent with terminology used by Ye et al. [13], three dimensionless parameters can be constructed from the following three independent solutions.

$$d^* = \frac{d}{a} = \begin{bmatrix} 1 \\ 0 \\ 0 \\ 0 \\ 0 \\ 0 \\ -1 \end{bmatrix} = -x_3$$

(25)

$$L_{th}^* = \frac{1}{Pe} = \begin{bmatrix} 0 \\ 0 \\ -1 \\ 1 \\ -1 \\ 0 \\ -1 \end{bmatrix} = -x_1 - x_3$$

(26)

$$\beta^* = \frac{AP}{h_m a D} = \begin{bmatrix} 0 \\ -1 \\ 0 \\ 1 \\ 0 \\ 1 \\ 1 \end{bmatrix}$$

(27)

Dimensionless parameters of Eqs. (25), (26), and (27) are very similar to dimensionless parameters of Eqs. (11), (12), and (13) developed by Ye et al. [13].

Appendix B: Experimental Measurements Error

Lane et al. [32] discusses the uncertainty of melt pool depth and width measurements from optical images. The main sources of uncertainty include the optical resolution, variability along the track length, user selection, and the standard uncertainty of the mean for repeat measurements. The variability along the track tends to be the largest component (e.g., 5%), and the variability in depth tends to be higher than the width (e.g., 2%).
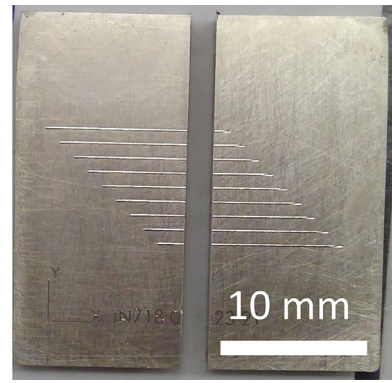
Fig. 11 Top view image of cross-sectioned plate with nine repeat tracks (Power = 285 W, Speed = 960 mm/s, Spot diameter = 80 μm)

The variation in melt pool depth depends on the process parameters. The greatest variation in melt pool depth along the length of the track is expected for unstable keyholing. King et al. [9] showed a variation in depth of ± 27% for a single laser track (316 stainless steel powder on a bare plate) under process conditions that created significant keyhole porosity defects (i.e., unstable keyholing). Another consideration is the transient regions at the start and end of the track. Shrestha and Chou [33] studied the transient regions during single tracks with powder and found these transient regions are typically contained to < 1 mm with a steady state region in between. In the absence of powder (i.e., bare plate scans), in a more stable process regime, and ignoring the transient regions at the start and end of tracks, we estimate the variation in depth to be significantly less at ± 5%. This was confirmed to be a reasonable estimate based on repeat tracks cross-sectioned at multiple locations. Figure 11 shows an example of repeat tracks measured at different locations along the scan distance. Melt pool depth and width were measured on both halves (n = 18 for each measurand). The average %standard deviation depth and width were 141.3 μm ± 2.7 μm and 122.4 μm ± 2.1 μm, respectively. Porosity defects caused by unstable keyholing were not observed for any of the process parameters in this study. No cross sections were taken in the transient regions at the start and end of tracks.

Declarations

Conflict of Interest The authors declare that they have no conflict of interest.

References

1. Bourell D, Coholich J, Chalancon A, Bhat A (2017) Evaluation of energy density measures and validation for powder bed fusion of polyamide. CIRP Ann 66(1):217–220
2. Mukherjee T, Manvatkar V, De A, DebRoy T (2017) Dimensionless numbers in additive manufacturing. J Appl Phys 121(6):064904
3. Wang L, Wei QS, Shi YS, Liu JH, He WT (2011) Experimental investigation into the single-track of selective laser melting of IN625. In: Advanced materials research, vol 233, pp 2844–2848. Trans Tech Publ
4. Ciurana J, Hernandez L, Delgado J (2013) Energy density analysis on single tracks formed by selective laser melting with CoCrMo powder material. Int J Adv Manuf Technol 68(5):1103–1110
5. Yadroitsev I, Yadroitsava I, Bertrand P, Smurov I (2012) Factor analysis of selective laser melting process parameters and geometrical characteristics of synthesized single tracks. Rapid Prototyping J
6. Bertoli US, Wolfer AJ, Matthews MJ, Delplanque J-PR, Schoenung JM (2017) On the limitations of volumetric energy density as a design parameter for selective laser melting. Mater Des 113:331–340
7. Weaver JS, Heigel JC, Lane BM (2022) Laser spot size and scaling laws for laser beam additive manufacturing. J Manuf Process 73:26–39
8. Hann DB, Iammi J, Folkes J (2011) A simple methodology for predicting laser-weld properties from material and laser parameters. J Phys D Appl Phys 44(44):445401
9. King WE, Barth HD, Castillo VM, Gallegos GF, Gibbs JW, Hahn DE, Kamath C, Rubenchik AM (2014) Observation of keyhole-mode laser melting in laser powder-bed fusion additive manufacturing. J Mater Process Technol 214(12):2915–2925
10. Hanemann T, Seyfert C, Holfelder P, Rota A, Heilmaier M (2020) Dimensionless enthalpy as characteristic factor for process control in laser powder bed fusion. J Laser Micro Nanoeng 15(3):257–266
11. Rubenchik AM, King WE, Wu SS (2018) Scaling laws for the additive manufacturing. J Mater Process Technol 257:234–243
12. Fabbro R (2019) Scaling laws for the laser welding process in keyhole mode. J Mater Process Technol 264:346–351
13. Ye J, Khairallah SA, Rubenchik AM, Crumb MF, Guss G, Belak J, Matthews MJ (2019) Energy coupling mechanisms and scaling behavior associated with laser powder bed fusion additive manufacturing. Adv Eng Mater 21(7):1900185
14. Eagar TW, Tsai NS et al (1983) Temperature fields produced by traveling distributed heat sources. Weld J 62(12):346–355
15. Buckingham E (1914) On physically similar systems; illustrations of the use of dimensional equations. Phys Rev 4(4):345
16. Grossmann A, Felger J, Froelich T, Gosmann J, Mittelstedt C (2019) Melt pool controlled laser powder bed fusion for customised low-density lattice structures. Mater Des 181:108054
17. Großmann A, Mölleney J, Frölich T, Merschroth H, Felger J, Weigold M, Sielaff A, Mittelstedt C (2020) Dimensionless process development for lattice structure design in laser powder bed fusion. Mater Des 194:108952
18. Yang Y, Großmann A, Kühn P, Mölleney J, Kropholler L, Mittelstedt C, Bai-Xiang X (2022) Validated dimensionless scaling law for melt pool width in laser powder bed fusion. J Mater Process Technol 299:117316
19. Gan Z, Kafka OL, Parab N, Zhao C, Fang L, Heinonen O, Sun T, Liu WK (2021) Universal scaling laws of keyhole stability and porosity in 3D printing of metals. Nat Commun 12(1):1–8
20. Coen V, Goossens L, Van Hooreweder B (2022) Methodology and experimental validation of analytical melt pool models for laser powder bed fusion. J Mater Process Technol, p 117547
21. Simonds BJ, Tanner J, Artusio-Glimpse A, Williams PA, Parab N, Zhao C, Sun T (2021) The causal relationship between melt pool geometry and energy absorption measured in real time during laser-based manufacturing. Appl Mater Today 23:101049
22. Wang Z, Liu M (2019) Dimensionless analysis on selective laser melting to predict porosity and track morphology. J Mater Process Technol 273:116238
23. Goossens LR, Van Hooreweder B (2021) A virtual sensing approach for monitoring melt-pool dimensions using high speed coaxial imaging during laser powder bed fusion of metals. Addit Manuf 40:101923
24. Liu B, Fang G, Lei L (2021) An analytical model for rapid predicting molten pool geometry of selective laser melting (SLM). Appl Math Model 92:505–524
25. Rankouhi B, Agrawal AK, Pfefferkorn FE, Thoma DJ (2021) A dimensionless number for predicting universal processing parameter boundaries in metal powder bed additive manufacturing. Manuf Lett 27:13–17
26. Agrawal AK, Rankouhi B, Thoma DJ (2022) Predictive process mapping for laser powder bed fusion: a review of existing analytical solutions. Curr Opin Solid State Mater Sci 26(6):101024
27. Rai R, Elmer JW, Palmer TA, DebRoy T (2007) Heat transfer and fluid flow during keyhole mode laser welding of tantalum, Ti–6Al–4V, 304L stainless steel and vanadium. J Phys D Appl Phys 40(18):5753
28. Trapp J, Rubenchik AM, Guss G, Matthews MJ (2017) In situ absorptivity measurements of metallic powders during laser powder-bed fusion additive manufacturing. Appl Mater Today 9:341–349
29. Simonds BJ, Sowards J, Hadler J, Pfeif E, Wilthan B, Tanner J, Harris C, Williams P, Lehman J (2018) Time-resolved absorptance and melt pool dynamics during intense laser irradiation of a metal. Phys Rev Appl 10(4):044061
30. Deisenroth DC, Mekhontsev S, Lane B (2020) Measurement of mass loss, absorbed energy, and time-resolved reflected power for laser powder bed fusion. 11271:112710L
31. Lane B, Mekhontsev S, Grantham S, Vlasea ML, Whiting J, Yeung H, Fox J, Zarobila C, Neira J, McGlauflin M (2016) Design, developments, and results from the NIST additive manufacturing metrology testbed (AMMT). In: 2016 International solid freeform fabrication symposium. University of Texas at Austin
32. Lane B, Heigel J, Ricker R, Zhirnov I, Khromschenko V, Weaver J, Phan T, Stoudt M, Mekhontsev S, Levine L (2020) Measurements of melt pool geometry and cooling rates of individual laser traces on IN625 bare plates. Integr Mater Manuf Innov 9(1):16–30
33. Shrestha S, Chou K (2021) A study of transient and steady-state regions from single-track deposition in laser powder bed fusion. J Manuf Process 61:226–235